Minimum-Phase Calibration of Sampling Oscilloscopes

Andrew Dienstfrey, Paul D. Hale, *Senior Member, IEEE*, Darryl A. Keenan, Tracy S. Clement, *Senior Member, IEEE*, and Dylan F. Williams, *Fellow, IEEE*

***Abstract*—We describe an algorithm for determining the minimum phase of a linear time-invariant response function from its magnitude. The procedure is based on Kramers–Kronig relations in combination with auxiliary direct measurements of the desired phase response. We demonstrate that truncation of the Hilbert transform gives rise to large errors in estimated phase, but that these errors may be approximated using a small number of basis functions. As an example, we obtain a minimum-phase calibration of a sampling oscilloscope in the frequency domain. This result rests on data obtained by an electrooptic sampling (EOS) technique in combination with a swept-sine calibration procedure. The EOS technique yields magnitude and phase information over a broad bandwidth, yet has degraded uncertainty estimates from dc to approximately 1 GHz. The swept-sine procedure returns only the magnitude of the oscilloscope response function, yet may be performed on a fine frequency grid from about 1 MHz to several gigahertz. The resulting minimum-phase calibration spans frequencies from dc to 110 GHz, and is traceable to fundamental units. The validity of the minimum-phase character of the oscilloscope response function at frequencies common to both measurements is determined as part of our analysis. A full uncertainty analysis is provided.**

***Index Terms*—Hilbert transform, Kramers–Kronig relation, linear response functions, minimum phase, mismatch correction, oscilloscopes.**

I. Introduction

At THE National Institute of Standards and Technology (NIST), Boulder, CO, we are developing high-speed electrical time- and frequency-domain metrology that is based on an electrooptic sampling (EOS) system that is traceable to fundamental physical units. A fundamental component of this metrology is a photodiode (PD) whose phase *and* magnitude response is calibrated in the frequency domain up to 110 GHz using the NIST EOS system [1]–[3]. The PD calibration includes corrections for the complex characteristic impedances of the measurement system, as well as dispersion and multiple reflections. Once calibrated, the PD can be used to calibrate high-speed electrical test equipment, including sampling oscilloscopes [4]. We will refer to this as the EOS-PD calibration of the oscilloscope.

The EOS system is designed for measurements requiring high bandwidths, 110 GHz or more at present, and has degraded uncertainty below several hundred megahertz due to the maximum time interval the system is capable of measuring. This gives rise to an uncertainty in the PD response that propagates into an increased uncertainty in the EOS-PD oscilloscope calibration over this same low-frequency regime. This is a serious impediment for using the oscilloscope to obtain calibrated waveforms over time intervals larger than roughly 1 ns or, conversely, spectral information below 1 GHz. Furthermore, it is difficult to obtain accurate absolute scaling for the voltage pulse generated by the PD [1]. Thus, the EOS-PD calibration alone cannot be used to give accurate absolute voltages, as measured by the oscilloscope.

As an alternative to the EOS-PD calibration, swept-sine (frequency-domain) measurements can be used to determine the magnitude of the frequency response of an oscilloscope, as described in [5] and [6]. The swept-sine calibration can be made at any frequency at which fundamental microwave power standards are available, typically from 0.1 MHz to greater than 50 GHz. However, since the swept-sine calibration does not give phase information, an oscilloscope calibrated using this technique alone is not adequately characterized for time-domain metrology.

In this paper, we describe a procedure for reconstructing the minimum phase of the oscilloscope response function from its magnitude. Minimum-phase response functions have the property that, in principal, the phase can be recovered from the Hilbert transform of the logarithm of the magnitude [7]. In practice, naive attempts to apply the standard theory can yield extremely large absolute errors in the computed phase. This is due to the truncation of the required integral operators to the necessarily finite bandwidths attainable by measurement. Variations of this problem are well known and have been discussed previously by several authors, [8]–[11].

Our fundamental observation is that although the truncation error may be large in absolute scale, due to the localizing nature of the Hilbert transform, this error is inherently low rank in the sense that it can be approximated by a small number of customized basis functions. As we have independent and direct measurements of the phase response supplied by the EOS-PD calibration over a large bandwidth, we solve a linear least squares problem for the difference between our measured values of the phase and the values computed via a minimum-phase assumption as an expansion in our specialized basis. This expansion corrects the absolute size and coarse trends in the truncated minimum-phase approximation. We provide a complete uncertainty analysis of the procedure.

Naturally, the final goal of a calibration is to determine the *true* frequency-domain response, which may or may not be min-

Manuscript received December 15, 2005; revised March 14, 2006.

The authors are with the National Institute of Standards and Technology, Boulder, CO 80305 USA (e-mail: andrewd@boulder.nist.gov; hale@boulder.nist.gov).

Digital Object Identifier 10.1109/TMTT.2006.879167

imum phase. In our example, our analysis allows us to conclude that the oscilloscope response function is indeed minimum phase over the bandwidth attainable by direct EOS-PD measurements.[1] Although the minimum-phase property would seem desirable for an oscilloscope, given that such response functions optimize a form of energy transfer (see, e.g., [12]), we have not seen such a claim made before in the literature. To the contrary, there exist several possible physical mechanisms [13] that could, in principle, lead to a nonminimum phase response.

For theoretical reasons and based on experiments we have performed in the laboratory, we conjecture that the minimum-phase character of the oscilloscope response extends into the low-frequency region. If so, our analysis results in a traceable extension of the oscilloscope calibration to frequencies below those unattainable by our present EOS techniques. Space does not permit these arguments to be made in their entirety below.

To be clear, the results contained in this paper are as follows.

1) We describe an algorithm for correcting for truncation effects in minimum-phase analysis with a full description of error propagation,
2) We present a new uncertainty analysis for the swept-sine calibration procedure introduced in [5] and [6],
3) We demonstrate that the oscilloscope response function is given by the minimum-phase response from 1 to 100 GHz.

A brief description of this paper follows. In Section II, we present the minimum-phase analysis and derive the basis functions suitable for correcting truncation effects. Section III contains our uncertainty analyses of the swept-sine calibration and the minimum-phase reconstruction. In Section IV, we implement the procedure to calibrate a high-speed equivalent-time sampling oscilloscope in the frequency domain. Finally, the assumption that the oscilloscope response function is minimum phase is fundamental to our analysis. We return to this in the conclusion presented in Section V. The swept-sine calibration of the oscilloscope magnitude was described previously in [5] and [6]. An abbreviated description is included here in Appendix A for completeness. The uncertainty analysis for this calibration appearing in Section III of this paper is new. We also include various numerical details in Appendix B, again for completeness.

Throughout this paper, we use the "pseudowave" formalism of [14] to characterize signals in microwave networks and limit our discussion to frequencies below the cutoff frequency of the guiding structures. Furthermore, the desired instrument responses are assumed to be linear and time invariant, and also to satisfy the necessary technical constraints; e.g., they are finite square integrable, unless otherwise noted.

II. Phase Reconstruction

Here, we describe the theory and implementation of the minimum-phase analysis.

[1]Technically the minimum-phase property is a global one in the frequency domain. Phrases referring to the minimum-phase character of a frequency-domain response function over a finite bandwidth are to be understood as a lack of observable features attributable to Blaschke terms in the fully general factorization of (1).

A. Theory

An arbitrary frequency-domain response function can be factored as [12]

$$h(f) = \tilde{h}(f)\exp(j2\pi f\tau)B(f) \tag{1}$$

where $\tilde{h}(f)$ is the minimum-phase response, τ is a real time offset, and $B(f)$ is a Blaschke product or "all-pass filter." One distinguishing characteristic of a minimum-phase function is that its phase is determined by its magnitude via a Hilbert transform relationship. There are various ways to express this; for our purposes, the most elementary version is sufficient. Writing $\tilde{h}(f) = |\tilde{h}(f)|\exp(j\phi(f))$, we have

$$\phi(f) = \frac{2f}{\pi}\int_0^\infty \frac{1}{f^2 - s^2}\ln(|\tilde{h}(s)|)ds. \tag{2}$$

One recognizes (2) as the usual Kramers–Kronig relations applied to the real and imaginary parts of the function $\ln(\tilde{h}) = \ln|\tilde{h}| + j\phi$. The analyticity of $\ln(\tilde{h})$ and consequent applicability of (2) is equivalent to the minimum-phase constraint. Note, by definition, a minimum-phase response has neither delay, nor all-pass components $\tau = 0$ and $B(f) = 1$. Currently we are unable to determine an absolute time origin. Therefore, we refer to response functions with possibly nonzero τ as minimum phase even though this is incorrect, strictly speaking.

A pervasive problem in the application of any Kramers–Kronig analysis is to estimate the error due to the finite bandwidth of a measurement. As it is impossible to measure to infinite frequency, in practice, the integral in (2) is truncated. We define

$$\phi_\Omega(f) = \frac{2f}{\pi}\int_0^\Omega \frac{1}{f^2 - s^2}\ln(|\tilde{h}(s)|)ds. \tag{3}$$

where Ω is the maximum frequency attainable by experiment. The problem is to estimate the effects of integrating only out to Ω [8], [9], [11]. (We use s as a dummy variable and it should not be confused with the usual Laplace transform argument.)

Concerning this truncation effect, there is a significant distinction between phase recovery and the use of Kramers–Kronig relations to relate real and imaginary parts of response functions. As the time-domain impulse response functions of interest are real, standard parity arguments from Fourier analysis imply that the magnitudes of the frequency-domain response functions roll off as some even power, $|h(f)| = O(|f|^{-2n})$ at large frequencies. Experimentally, the magnitudes of generic oscilloscope response functions have been observed to decay like $1/f^2$, i.e., $n = 1$ [15]. Regardless, as we will see, our results are independent of n. We assume an asymptotic expansion of the form

$$|h(f)| = \frac{H_{2n}}{f^{2n}}\left(1 + \frac{\gamma_2}{f^2} + \frac{\gamma_4}{f^4} + \cdots\right) \tag{4}$$

where H_{2n} and the γ's are constants. For fixed f, such that $|f| < \Omega$, a simple estimate gives

$$\begin{aligned}\left|\frac{2f}{\pi}\int_{\Omega}^{\infty}\frac{1}{f^2-s^2}\ln(|\tilde{h}(s)|)\,ds\right| &\le C\int_{\Omega}^{\infty}\frac{1}{s^2}\left(1+\frac{f^2}{s^2}+\cdots\right)\left|\ln\left(\frac{H_{2n}}{s^{2n}}(1+\cdots)\right)\right|ds\\ &\le C\int_{\Omega}^{\infty}\left[2n\frac{\ln(s)}{s^2}+(1+\ln(H_{2n}))\frac{1}{s^2}+\cdots\right]\\ &\le C\frac{\ln(\Omega)}{\Omega}. \end{aligned} \tag{5}$$

In this set of equations, the constant C depends on n and is allowed to change from line to line. The ellipses represent series terms in higher inverse powers of s and, therefore, may be ignored asymptotically. Notice that the form of the estimate is independent of the rate of rolloff of the frequency-domain response function, i.e., n. The point here is that the scaling $\ln(\Omega)/\Omega$ converges so weakly as to not be useful. The implication is that even if the minimum phase hypothesis is valid, it is difficult to compute an estimate of the underlying minimum phase regardless of the experimental bandwidth.

The situation is radically different when attempting to recover the imaginary from the real part. Using the same approach as in (5) yields an estimate of the truncation error (again assuming fixed $|f| < \Omega$), which is

$$\left|\frac{2f}{\pi}\int_{\Omega}^{\infty}\frac{1}{f^2-s^2}\mathrm{Re}(h(s))ds\right| \le \frac{C}{\Omega^{2n+1}}. \tag{6}$$

In this case, given a fixed interval of target frequencies, the size of the error due to truncation approaches zero rapidly as the measurement bandwidth increases.

An example of these estimates may be instructive. Consider the second-order low-pass Butterworth filter given by

$$h(f) = \frac{1}{1-j\sqrt{2}f-f^2}. \tag{7}$$

As a low-pass filter with $1/f^2$ rolloff, (7) is a reasonable surrogate for an oscilloscope response function for which the 3-dB frequency point has been normalized to be $f = 1$ (see [15]). We emphasize that our results rely neither on this class of filters, nor the order. The Butterworth filter is minimum phase, thus, (2) is valid. For fixed target frequency $f = 1/3$, we compute the functions

$$\begin{aligned} h(1/3) &= 0.878048780 + j\,0.46565568\\ \ln(h(1/3)) &= -0.00613504 + j0.48761624. \end{aligned}$$

Consider the evaluation of $\mathrm{Im}(h_\Omega(1/3))$ and $\phi_\Omega(1/3) = \mathrm{Im}[\ln(h)]$ from $\mathrm{Re}(h(f))$ and $\ln(|h(f)|) = \mathrm{Re}[\ln(h)]$, respectively, using truncated integrals of the form (3). Computing the required Hilbert transforms for different truncation frequencies gives the results of Table I.

TABLE I
VALUE OF IMAGINARY PART AND PHASE OF RECONSTRUCTED FUNCTION $h_\Omega(1/3)$ FOR DIFFERENT TRUNCATION FREQUENCIES Ω

Ω	$\mathrm{Im}(h_\Omega(1/3))$	$\phi_\Omega(1/3)$
2	0.4582043	0.126
5	0.4651023	0.266
10	0.4655853	0.347
100	0.4656556	0.464
1000	0.4656557	0.484

If the real part is measured to twice the 3-dB frequency, we observe two-digit accuracy on the calculated imaginary part. By contrast, corresponding accuracy in the calculated phase requires magnitude measurements out to 1000 times the characteristic frequency. This slow convergence is consistent with the estimate given in (5).

It is clear that estimation of the phase of a minimum-phase response function from (3) alone will exhibit large errors due to the truncation of the integral. However, we claim that although this error is large in magnitude, it is simultaneously low rank. By "low rank" we mean that it will be possible to expand the difference between the minimum phase and the phase computed by the truncated operator (3) in terms of a small number of functions that we define specially for this purpose.

B. Definition of Basis Functions

We assume that the response is minimum phase with the exception of a possible unknown time shift τ. In this case, (2) holds with a slight modification

$$\begin{aligned}\phi(f) &= \frac{2f}{\pi}\int_{0}^{\infty}\frac{1}{f^2-s^2}\ln(|h(s)|)ds + 2\pi f\tau\\ &= \phi_\Omega(f) + \Delta(f)\end{aligned} \tag{8}$$

where $\phi_\Omega(f)$ is given by the truncated integral (3). The function $\Delta(f)$, defined implicitly by (8), is given by either of the equivalent expressions

$$\begin{aligned}\Delta(f) &= \phi(f) - \phi_\Omega(f)\\ &= \frac{2f}{\pi}\int_{\Omega}^{\infty}\frac{1}{f^2-s^2}\ln(|h(s)|)ds + 2\pi f\tau.\end{aligned} \tag{9}$$

Note that Δ encapsulates all unknown information of ϕ due to both finite bandwidth measurements and unknown time shift. As stated above, we know that $|h(f)|$ admits an asymptotic expansion in even powers of $1/f$. Assume that it is sufficient to keep only the first term of this expansion. Substituting this into the operator (9) gives

$$\begin{aligned}\Delta(f) &\approx c_1 f + c_2 f\int_{\Omega}^{\infty}\frac{1}{f^2-s^2}ds\\ &\quad + c_3 f\int_{\Omega}^{\infty}\frac{1}{f^2-s^2}\ln(s)ds\\ &= C_1\psi_1(f) + C_2\psi_2(f) + C_3\psi_3(f)\end{aligned} \tag{10}$$

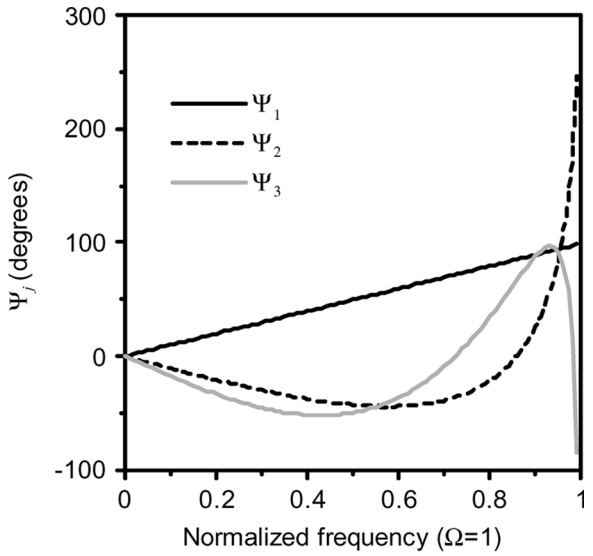

Fig. 1. Plot of orthonormal basis functions $(1/\sqrt{\Omega})\Psi(f/\Omega)$.

where the constants depend on τ, n, and H_{2n}. The functions ψ are

$$\begin{aligned}\psi_1(f) &= f \\ \psi_2(f) &= \ln\left(\frac{\Omega+f}{\Omega-f}\right) \\ \psi_3(f) &= f\Phi\left(\frac{f^2}{\Omega^2}, 2, \frac{1}{2}\right)\end{aligned} \tag{11}$$

where $\Phi(z,s,a)$ is the Lerch transcendent. The equation for ψ_3 is derived by expressing $1/(f^2-s^2)$ under the integral as a power series in f, integrating term by term, and rescaling the result to obtain the power series definition of $\Phi(z,s,a)$ [16]. This transcendent is a special function in the generalized Riemann–Zeta family and may be evaluated wherever needed either by the power series or its analytic continuation [16].

For conditioning purposes, it is preferable not to use these functions, but rather their orthogonalization given by a continuous version of the Gram–Schmidt procedure [17]. We denote the orthonormal functions by $\{\Psi_1, \Psi_2, \Psi_3\}$. They are shown for the case $\Omega = 1$ in Fig. 1. The case for general Ω is obtained through a suitable rescaling. For a more technical analysis of truncation effects relevant to the application of Kramers–Kronig procedures in the classical setting—e.g., recovery of the imaginary part from the real—see [9].

C. Procedure

We now have the tools necessary to describe our procedure. We assume that we have a reasonably dense sampling of magnitude measurements $|h(f_n)|$ and direct measurements of the phase $\phi_{\mathrm{EOS}}(f'_m)$. The magnitude measurements are obtained from the EOS-PD measurement of [4] and the swept-sine measurement described in Appendix A. The magnitude data sets, acquired on different frequency grids, are merged using the method described in Appendix B. The frequencies at which the phase is measured $\{f'_m \,|\, m = 1, \ldots, M\}$ need not be the same as those of the magnitude measurements $\{f_n \,|\, n = 1, \ldots, N\}$, nor even as dense. All that is required is that

$$\mathrm{Min}\{f_n\} \le \mathrm{Min}\{f'_m\} < \mathrm{Max}\{f'_m\} < \mathrm{Max}\{f_n\}.$$

Informally, the frequencies for which we have magnitude data should "cover" the frequencies associated with the phase measurements. For technical reasons, we enforce that the second of the two inequalities is strict (see Appendix B). We assume that the desired phase response is minimum phase, i.e., it satisfies (8), and that $\phi_{\mathrm{EOS}}(f'_m)$ is equal to a discrete sampling of $\phi(f)$.

Using the magnitude measurements, we evaluate $\phi_\Omega(f'_m)$, the truncated minimum-phase function (3) at all frequencies for which we have measured phase data. For discretization of the singular integrals, we represent the logarithms of the measured magnitude data as a piecewise linear function of frequency. The singular integral (3) is applied analytically to each of the linear segments and then re-summed outside the integral. The operator is evaluated at all of the frequencies where the EOS-PD calibration returns direct measurements of the phase response, as described in Appendix B. The result is a dense matrix $\mathbf{K}(f'_m, f_n)$ of order $M \times N$, where M is the number of EOS-PD data points and N is the total number of magnitude measurements. The fully discretized version of (3) reads

$$\phi_\Omega(f'_m) = \mathbf{K}(f'_m, f_n)\mathbf{h} \tag{12}$$

where $\mathbf{h}$ is the vector of logarithms of the magnitude response measurements.

Next we form the difference (9) at the frequencies of the EOS measurements

$$\Delta(f'_m) = \phi_{\mathrm{EOS}}(f'_m) - \phi_\Omega(f'_m). \tag{13}$$

Following (10), we make the ansatz

$$\Delta(f'_m) = \alpha_1\Psi_1(f'_m) + \alpha_2\Psi_2(f'_m) + \alpha_3\Psi_3(f'_m) \tag{14}$$

and solve for the undetermined coefficients $\alpha_1, \alpha_2, \alpha_3$ in a least squares sense. Our fundamental claim is that although $\Delta(f'_m)$ is large relative to the true underlying phase $\phi_{\mathrm{EOS}}(f'_m)$, the functional form (14) will be sufficient to expand Δ. This will be true if and only if the underlying response function is minimum phase. Thus, violations of this claim may be used as a test of the minimum-phase character of the measured response. We return to this below.

Finally, given sufficiently low residual in the least squares fit, an indicator of the validity of the minimum-phase assumption, we compute the phase of the oscilloscope response function as the sum

$$\phi_{\mathrm{mp}}(f) = \mathbf{K}(f, f_n)\mathbf{h} + \alpha_1\Psi_1(f) + \alpha_2\Psi_2(f) + \alpha_3\Psi_3(f). \tag{15}$$

In this equation, the domain of the Kramers–Kronig operator consists of the same frequencies as the magnitude measurements $\{f_n\}$; the target frequencies f are some arbitrary desired frequency grid.

III. Uncertainty Analysis

We perform a complete uncertainty analysis for the swept-sine measurement procedure and minimum-phase recovery algorithm. We recall the standard linearized propagation of errors. Given a scalar random variable $\mathbf{X}$ with mean $E(\mathbf{X}) = \mathbf{X}_0$ and variance $\mathrm{var}(\mathbf{X}) = u^2[\mathbf{X}]$, and variable $\mathbf{Y} = F(\mathbf{X})$, where F is sufficiently differentiable, we assume that

$$E[\mathbf{Y}] = F(\mathbf{X}_0)$$
$$u^2[\mathbf{Y}] = \left(\left. \frac{\partial F}{\partial s} \right|_{s=\mathbf{X}_0} \right)^2 u^2[\mathbf{X}]. \tag{16}$$

The multivariate analog involving the Jacobian of F is straightforward; details may be found in [18]. In most instances, we use the above formulas for computation of uncertainties. The one exception is the determination of the uncertainty in the mismatch factors in (29) or (30). In this case, the functional forms are sufficiently complex that we instead use Monte Carlo analysis to determine the uncertainties as functions of the constitutive reflection coefficients and S-parameters.

A. Swept-Sine Calibration

We find the uncertainty in $|h|$, as determined by the swept-sine calibration, by propagation of the uncertainties in (29) or (30) (of Appendix A), as appropriate. In linear units, we find the uncertainty in the magnitude of the impulse response spectrum as

$$u^2[|h|] = \left(\frac{1}{2}\right)^2 \left\{ \left(\frac{h}{P_\mathrm{s}}\right)^2 u^2[P_\mathrm{s}] + \left(\frac{h}{P_\mathrm{L}}\right)^2 u^2[P_\mathrm{L}] + \left(\frac{h}{P'_\mathrm{L}}\right)^2 u^2[P'_\mathrm{L}] + \left(\frac{h}{P_\mathrm{m}}\right)^2 u^2[P_\mathrm{m}] + \left(\frac{h}{k}\right)^2 u^2[k] + \left(\frac{h}{Q}\right)^2 u^2[Q] \right\} \tag{17}$$

where $u[\cdot]$ is the standard uncertainty of the quantity in brackets, and Q is the mismatch term on the right-hand side of either (29) or (30). All other terms in (17) are defined in Appendix A.

We estimate the uncertainty in each of the power measurements as the standard deviation of the mean of the measurements. The standard uncertainty in the calibration factor k is taken from either the manufacturer's specifications or the NIST calibration report for the power meter. The standard uncertainty in Q is determined from a Monte Carlo simulation that includes uncertainty in the magnitude and phase of all the scattering parameters. Uncertainty in the reflection coefficients in Q is determined from either: 1) the manufacturers specifications for the vector network analyzer used for the measurement or 2) NIST calibration reports. The scattering parameters of the adapter are determined from the Monte Carlo simulation of method described in [19], and includes uncertainties in the definitions of the open, short, and load terminations and the network analyzer manufacturer's specifications. Applying this analysis, we obtain that the standard uncertainty [18] of our swept-sine data is typically between 0.05–0.08 dB.

B. Minimum-Phase Computation

We propagate errors through the minimum-phase reconstruction in a sequence of steps. First we evaluate $\phi_\Omega(f'_m)$ via the truncated Hilbert transform (12). Using the rules for linear propagation of errors, we find that

$$u^2[\phi_\Omega] = \mathbf{K} \Sigma_{\mathbf{u}^2[\mathbf{h}]} \mathbf{K}^* \tag{18}$$

where $\Sigma_{\mathbf{u}^2[\mathbf{h}]}$ is the diagonal matrix containing the uncertainties (systematic and random) of the vector $\mathbf{h}$. (*Note*: this matrix could contain covariance estimates in off-diagonal terms if such information is available. These correlations are important for time-domain applications. See, e.g., [20].)

Next we form $\Delta(f'_m)$, the difference between the EOS-PD determined phase ϕ_EOS and ϕ_Ω (12). Since the EOS and swept-sine measurements are independent, the uncertainties $u^2[\phi_\mathrm{EOS}]$ and $u^2[\phi_\Omega]$ are added in quadrature.

The least squares problem (14) is then solved for the vector of coefficients $\boldsymbol{\alpha} = \{\alpha_1, \alpha_2, \alpha_3\}$. As with any linear least squares problem, the error in the solution vector $\boldsymbol{\alpha}$ will scale with the condition number of the underlying system matrix. In our case, this system matrix is given by

$$A_{mj} = \Psi_j(f'_m). \tag{19}$$

It is at this point that we benefit from having pre-orthogonalized the natural set of expansion functions $\{\psi_j\}$ (11) to instead form the orthonormal basis $\{\Psi_j\}$. Using the set $\{\Psi_1(f), \Psi_2(f), \Psi_3(f)\}$ to define $\mathbf{A}$ in place of the naïve functions (11) reduces the condition number of $\mathbf{A}$ from over 100 to around unity. Another way to view this is that, as the Ψ_j are orthonormal in a continuous sense, the discretized least squares solution of (14) effectively is given by a well-conditioned projection.

Finally, we evaluate $\phi_\mathrm{mp}(f)$ wherever desired as the sum (15). In principle, there exist correlations between the coefficients α_j and the Kramers–Kronig operator applied to the magnitude measurements, given that the later appear in the evaluation of the initial phase estimate ϕ_Ω. We assume these to be negligible, as we require the values of $\phi_\mathrm{mp}(f)$ at precisely those frequencies where the EOS-PD calibration yields unreliable phase measurements. For this reason, whatever correlations exist between the phase contributions of $\mathbf{K}(f, f_n)\mathbf{h}$ and the coefficients α_j would have to be effected through the off-diagonal components of the Kramers–Kronig operator and subsequent least-squares analysis. We assume these to be insignificant. Therefore, in this final expression for $\phi_\mathrm{mp}(f)$ the relevant random variables are $\mathbf{h}$ and the set $\{\alpha_1, \alpha_2, \alpha_3\}$, which, by this argument, are independent. The error propagation through the integral operator and the three pointwise multiplications obey their respective linear propagation formalisms, and the resulting uncertainties of each are added in quadrature.

IV. Oscilloscope Calibration

We implemented the procedures outlined above to obtain a minimum-phase calibration of our equivalent-time high-speed

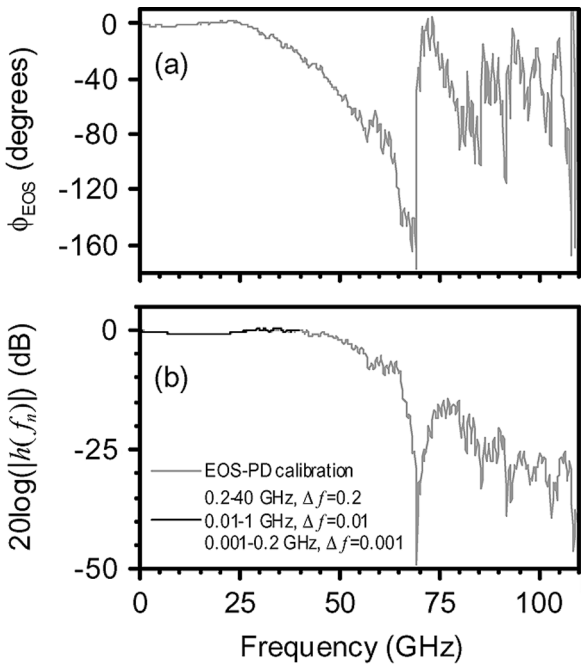

Fig. 2. EOS-PD calibration: (a) phase and (b) magnitude are shown in grey. Black lines show three separate sets of swept sine measurements. Together, measurements span a five decade frequency range.

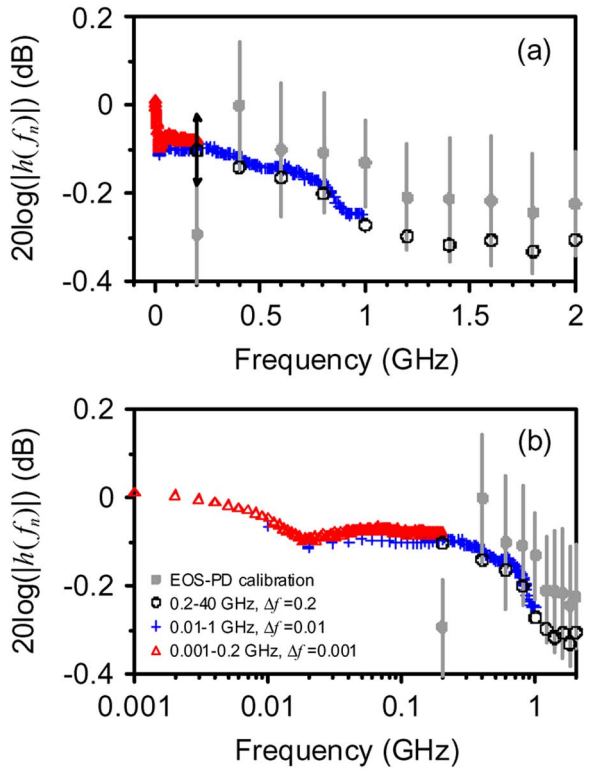

Fig. 3. Plot of the magnitude measurements from the EOS-PD calibration and three swept-sine experiments. The combined uncertainty in the swept-sine measurements is generally between 0.05–0.08 dB (the black error bar, shown for scale, is ±0.08 dB.) Uncertainties for the EOS-PD calibration is shown as gray error bars. (Color version available online at: http://ieeexplore.ieee.org.)

sampling oscilloscope. This oscilloscope has a nominal bandwidth of approximately 50 GHz and has an adapter to convert from the oscilloscope's usual 2.4-mm connector to a 1.0-mm coaxial input. It is at this 1.0-mm input reference plane that we calibrate.

In our current configuration, the EOS-PD oscilloscope calibration gives the magnitude and phase of the oscilloscope response function at the 1.0-mm coaxial reference plane $h(f)$ on an equi-spaced frequency grid from 200 MHz to 110 GHz in 200-MHz increments. These data are shown in Figs. 2 and 3. An uncertainty analysis, performed as part of that calibration, is given in [4]. In addition to the sources of error identified in that analysis, we also expect an increase in the uncertainty at low frequencies due to the limited time interval that is measured by the EOS platform currently used to calibrate the PD. As the oscilloscope is capable of taking measurements over large time windows, e.g., longer than 5 ns, the low frequency cutoff at 200 MHz is insufficient for utilizing the oscilloscope in the manner that it could potentially be used.

To augment the EOS-PD calibration, swept-sine calibrations were performed at the oscilloscope's 2.4-mm input connector plane, and the calibration was then embedded behind the 1.0-mm adapter. The measurements and uncertainty analysis were performed as discussed in Appendix A and Section III, respectively. After all mismatch corrections have been made to account for adapter transfer and device reflections, these experiments return the response magnitude $|h(f)|$ on equi-spaced frequency grids. Separate calibrations were made with this technique over three overlapping frequency ranges.

Plots of the resulting magnitudes are shown in Figs. 2 and 3, along with details of the measured frequency grids in the inset.

In Fig. 3, we show the plots on both linear and logarithmic frequency scales so as to examine certain features in the data. The analysis of Section III-A yields a combined uncertainty in the swept-sine measurements of generally between 0.05–0.08 dB. A sample error bar is shown at the 0.20 GHz point in Fig. 3.

We draw attention to two features in these plots. First, the EOS-PD calibration at the lowest two points (0.200 and 0.400 GHz) does not follow the response trend as measured by the swept-sine technique. In fact, the 0.200-GHz point differs from the swept-sine measurements by almost twice the combined measurement uncertainties as based on our current uncertainty analysis of the EOS-PD calibration [4]. Although less pronounced, a similar discrepancy appears at the 0.400-GHz point. Due to these discrepancies and additional time-domain measurements we have performed, we conclude that our current uncertainty analysis of the EOS-PD calibration does not accurately capture the uncertainty due to the limited time interval that is measured by the EOS system. For the purposes of our current minimum-phase analysis, we neglect these two points as outliers.

Second, the notch feature in the magnitude response centered near 0.020 GHz, although small (∼0.1 dB), is both repeatable and large relative to the uncertainties as computed by our uncertainty analysis. Furthermore, this is a feature that would be missed entirely if one were to extrapolate the EOS-PD calibration to dc from the lowest EOS-PD frequency measurement of 0.200 GHz.

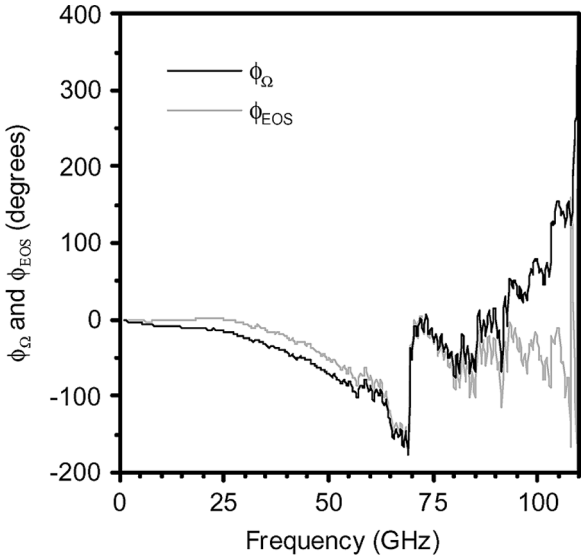

Fig. 4. Plot of the phase measured directly as part of the EOS-PD calibration $\phi_{\rm EOS}$ and the evaluation of the truncated Kramers–Kronig operator ϕ_Ω calculated from (12).

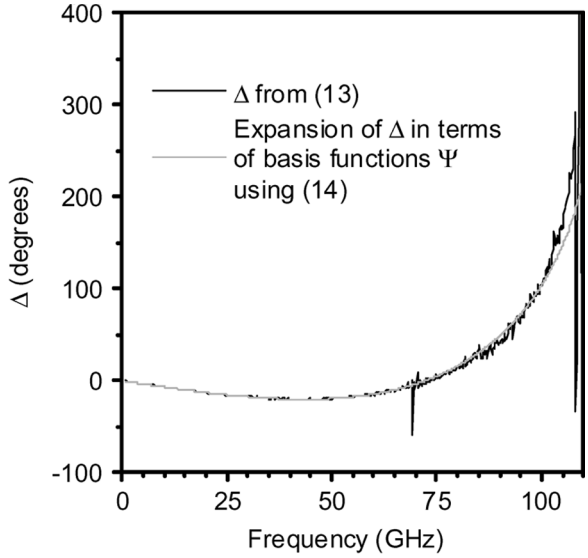

Fig. 5. Plot of the difference of the two curves in Fig. 4, Δ, and its expansion in the orthogonalized basis functions Ψ.

We proceed to the minimum phase computation. For magnitude data, we used a synthesis of the three swept-sine data sets and the magnitude data of the EOS-PD calibration. Our procedure for combining data sets is described in Appendix B. The result is a single vector of magnitude measurements on an irregular frequency grid spanning five decades of frequencies (from 1 MHz to 110 GHz). This is the grid: $\{f_n\}$.

Next, the truncated singular integral operator $\phi_\Omega(f'_m) = \mathbf{K}(f'_m, f_n)\mathbf{h}$ was computed at all frequencies f'_m of the EOS-PD data set with the composite product rule described in Appendix B. This result is shown along with the EOS-PD measured phase in Fig. 4. We observe that the fine-scale structures of the two curves agree. Simultaneously, there are gross trends that have not been accounted for. The quantity $\Delta(f'_m)$ is evaluated as the difference between these two curves and is shown in Fig. 5. The basis functions Ψ_j were tabulated at the same frequencies as $\Delta(f'_m)$ and the system was inverted in a least squares sense for the coefficients α_j. The resulting expansion of $\Delta(f'_m)$ in the basis of Ψ_j is shown as the smooth curve in Fig. 5. We observe that this expansion captures all significant features of $\Delta(f'_m)$; thus, we conclude that the minimum phase hypothesis is valid.

We evaluate the minimum-phase response at all of the fundamental frequencies as the sum of the singular integral operator and $\Delta(f)$ computed as a linear combination of $\Psi_j(f)$, as in (15). A plot over low frequencies of the measured phase and the minimum phase computed using our procedure is shown in Fig. 6. The standard uncertainties computed as in Section III-B are shown as the upper and lower dashed curves. The few EOS-PD measurements of phase lying below 2 GHz are included for comparison. The computed phase lies well within the EOS-PD measurement uncertainty. Note that the ~0.075-dB dip in magnitude centered at ~0.02 GHz (see Fig. 3) gives rise to the ~0.4° rising region between 0.01–0.03 GHz. We have indeed observed these features (magnitude and phase) in measurements of comb generators performed with this oscilloscope.

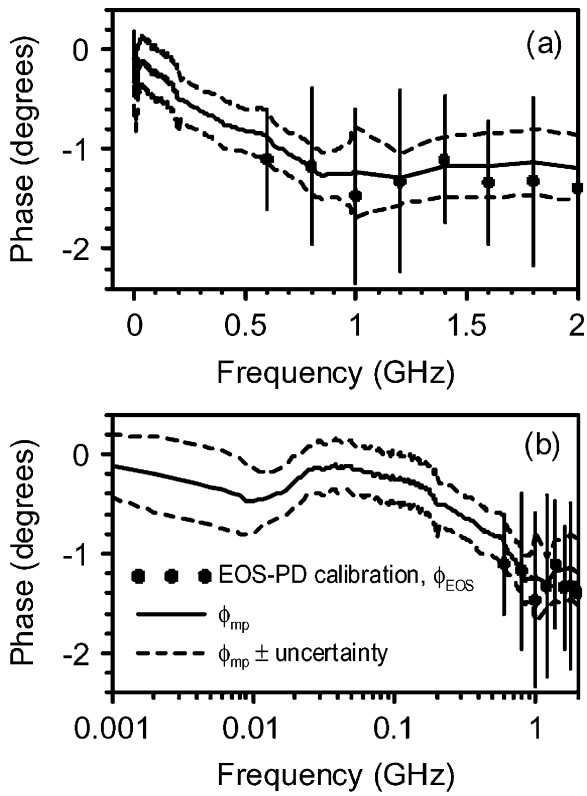

Fig. 6. Phase response of our oscilloscope estimated using the ESO-PD calibration and the minimum-phase procedure described in this study. Combined uncertainties for the minimum-phase estimate are shown as the dashed lines, while uncertainties in the EOS-PD calibration are shown as gray error bars.

Finally, in Fig. 7, we plot the difference between the phase measured directly by the EOS-PD calibration and the computed minimum phase over all frequencies of the EOS-PD data set. The uncertainty of the difference (which is dominated by the EOS-PD measurements) is represented by the shaded gray region in this figure. The difference is less than a few degrees for $f < 70$ GHz, and may be considered to be zero to within the

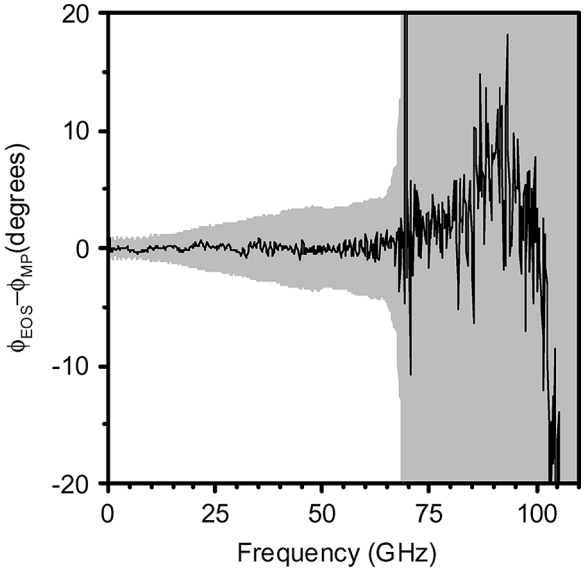

Fig. 7. Difference between phase measured directly by the EOS-PD calibration and the computed minimum phase, plotted for all frequencies of the EOS-PD data set. The uncertainty in the difference is represented by the gray shaded region.

reported uncertainties. For frequencies above 70 GHz, the difference still remains small although the uncertainties returned by the EOS-PD calibration become quite large due to the small magnitude of the response function in this region. From this, we conclude that the oscilloscope response function is indistinguishable from the minimum-phase response function over this bandwidth.

V. Conclusion

We have described a procedure for systematically eliminating the large error due to truncation effects in the implementation of a minimum-phase analysis. A complete analysis of error propagation has been performed. As an example, we augmented swept-sine and EOS-PD data sets so as to obtain a minimum-phase calibration of our oscilloscope response function at frequencies unattainable by either technique individually. In the process of this analysis, we observed that the true oscilloscope response function as measured by the EOS-PD calibration is indistinguishable from the minimum-phase response over a very large bandwidth. The theoretical possibility that the true response function is not minimum phase cannot be ruled out from the results and arguments presented above. However, based on subsequent measurements and analysis, we conjecture that this oscilloscope response is, within practical limits, minimum phase to frequencies lower than we can attain using our EOS-PD calibration. We stress that this last assertion applies to our particular model oscilloscope and may not be valid for other models of oscilloscopes or oscilloscopes made by other manufacturers. We will report on these results in the future.

Appendix A
Swept Sine Magnitude Measurement

A. Theory

A power sensor is commonly used to measure the power of a single-frequency microwave source, as described in [21]. When directly connected to the signal source, the power meter reading $P_{\rm m}$ is given by

$$P_{\rm m} = \frac{1}{2}\eta(|a|^2 - |b|^2) = \frac{1}{2}\eta|a|^2(1 - |\Gamma_{\rm m}|^2). \tag{20}$$

Here, a and b [shown schematically in Fig. 8(a)] are the forward and reverse wave amplitudes of the "pseudowaves" at the junction between the source and the power meter (or oscilloscope) and are normalized to a 50-Ω reference impedance (see [14]). These wave amplitudes have units of the square root of a watt.[2] The quantity $\Gamma_{\rm m}$ is the vector reflection coefficient of the power meter, and $1 - |\Gamma_{\rm m}|^2$, known as the mismatch loss, accounts for the power reflected by the sensor. The sensor efficiency η accounts for ohmic and radiation losses in the sensor interconnection and housing. Both factors are used to correct measured incident power in commercial power meters, and are usually combined in a calibration factor $k = \eta(1 - |\Gamma_{\rm m}|^2)$. From (20), we see that the calibrated power meter measures the power in the incident wave

$$\frac{P_{\rm m}}{k} = \frac{1}{2}|a|^2. \tag{21}$$

The net incident power can be related to the power the source would deliver to a 50-Ω load $(1/2)|b_g|^2$ by the relation

$$\frac{1}{2}|a|^2 = \frac{\frac{1}{2}|b_{\rm g}|^2}{|1 - \Gamma_{\rm m}\Gamma_{\rm g}|^2} \tag{22}$$

where $\Gamma_{\rm g}$ is the vector reflection coefficient of the source. Combining (20) and (22) gives the standard expression for the power the source would deliver to a 50-Ω load in terms of the power meter reading, the meter calibration factor, and the meter and generator reflection coefficients

$$\frac{1}{2}|b_{\rm g}|^2 = \frac{P_{\rm m}}{k}|1 - \Gamma_{\rm g}\Gamma_{\rm m}|^2. \tag{23}$$

By analogy with (21), we calibrate the oscilloscope so that it measures the incident a wave, as was used in earlier calibration methods [5]. That is, we calibrate the otherwise ideal[3] oscilloscope to measure the convolution of the incident wave with the oscilloscope impulse response and use a scale factor to give the voltage reading. In the frequency domain, this becomes a product

$$v_{\rm s} = ah\sqrt{50\ \Omega} \tag{24}$$

where h is the complex frequency response of the oscilloscope and is dimensionless, i.e., h is the transform of the impulse response of the oscilloscope evaluated at our frequency of interest,

[2]References [5], [14], and [21] use a root-mean-square (rms) normalization. The rms-normalized pseudowaves $\underline{a}$ and $\underline{b}$ are related to those used here, with $\underline{a} = a/\sqrt{2}$ and $\underline{b} = b/\sqrt{2}$.

[3]By "ideal" we mean that the oscilloscope is free from timing errors, nonlinearity, etc. We use the methods described in this study to characterize the finite-impulse response of the otherwise ideal oscilloscope. Compensation for other nonidealities is described in [4] and the cited references therein.

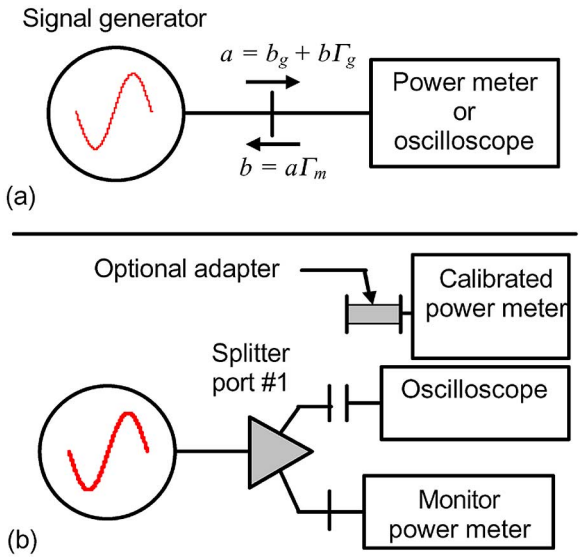

Fig. 8. Schematic diagram showing pseudowave definitions for power meter and oscilloscope calibration in (a) and experimental configuration in (b). (Color version available online at: http://ieeexplore.ieee.org.)

and v_s is the raw voltage measured by the oscilloscope. The scale factor $\sqrt{50\,\Omega}$ converts the pseudowave description to a voltage. For a more detailed analysis of this scaling, see [20].

Using an analysis similar to that leading to (22), the oscilloscope measurement can be related to the wave and power the source would deliver to a 50-Ω load

$$b_g = \frac{v_s}{h\sqrt{50\,\Omega}}(1 - \Gamma_g\Gamma_s) \tag{25}$$

and

$$\frac{1}{2}|b_g|^2 = \frac{\frac{1}{2}|v_s|^2}{(50\,\Omega)|h|^2}|1 - \Gamma_g\Gamma_s|^2 \tag{26}$$

where Γ_s is the vector reflection coefficient of the oscilloscope when in its quiescent state.

Since b_g is an invariant property of the signal generator, it can be used to relate the power meter and oscilloscope measurements. We equate (23) and (26) to give an expression for $|h|$ in terms of measured powers and reflection coefficients

$$|h|^2 = k\frac{P_s}{P_m} \cdot \frac{|1 - \Gamma_g\Gamma_s|^2}{|1 - \Gamma_m\Gamma_g|^2} \tag{27}$$

where $P_s = \frac{1}{2}|v_s|^2/(50\,\Omega)$.

B. Implementation

The configuration of the swept sine measurement system is shown in Fig. 8(b). The power at port 1 of the splitter is first measured by connecting directly to a calibrated power meter or, for low frequencies, a low-frequency power sensor is connected to port 1 through an adapter. The signal frequency is then stepped over the appropriate frequency range and, after allowing time for the equipment to settle, measurements are taken from the calibrated power meter and the monitor power meter.

Port 1 of the splitter is then connected directly to the oscilloscope and the oscilloscope is placed in a vertical histogram mode and is triggered asynchronously to measure the variance of the voltage at each frequency. We observe that this variance is the rms voltage measured by the oscilloscope. The power measured by the oscilloscope is calculated as

$$P_s = \frac{1}{50\,\Omega}\left(s_s^2 - s_b^2\right) \tag{28}$$

where s_s^2 is the measured signal variance and s_b^2 is the background variance measured with the signal generator turned off. The frequency of the signal generator is then stepped over the same frequency range, and the response of the oscilloscope is calculated as

$$|h| = \left[k\frac{P_s}{P_L'} \cdot \frac{P_L}{P_m} \cdot \frac{|1 - \Gamma_s\Gamma_g|^2}{|1 - \Gamma_m\Gamma_g|^2}\right]^{\frac{1}{2}} \tag{29}$$

where P_L is the monitor power meter reading while port 1 is connected to the calibrated meter and P_L' is the monitor reading when port 1 is connected to the oscilloscope. Using the ratio in (29) instead of (27) compensates for drift in the source power. When this type of ratio is used, the equivalent source reflection coefficient is found using the method described in [22].

In the case where the adapter is added to the power sensor, the response magnitude is calculated as

$$|h| = \left[k\frac{P_s}{P_L'} \cdot \frac{P_L}{P_m} \cdot \frac{|1-\Gamma_s\Gamma_g|^2|S_{21}|^2}{|1-S_{22}\Gamma_m-S_{11}\Gamma_g-\Gamma_m\Gamma_g\det(S)|^2}\right]^{\frac{1}{2}} \tag{30}$$

where S_{ij} are the scattering parameters of the adapter and $\det(S) = S_{11}S_{22} - S_{12}S_{21}$.

Appendix B
Numerical Details

Here we describe various numerical routines that were used for the computations above. We first present our algorithm for constructing a continuous description of tabulated noisy data. We refer to this procedure as "merging." Next we derive the analytic expressions representing the application of the singular integral operator (3) applied to the result of the discrete merged data as in (12). We stress that the analytic basis of our argument—that the discrepancy between a minimum phase response and the truncated Kramers–Kronig operator is low rank—is independent of discretization. By contrast, the error analysis presented above does depend on the discretization. The routines that we employ are general in that they do not require function data on a regular grid, and are robust to the presence of experimental noise. They are also low order, a feature which simplifies the algebra and error analysis considerably. There exist natural higher order analogs to the procedures that we outline. For our current applications, these were deemed unnecessary. We may consider implementing them in the future.

A. Merging

The Hilbert transform operator is very sensitive to sharp changes or discontinuities in the function to which it is being

applied. In our current application, such changes are inevitable as the magnitude data are obtained from different experiments over different frequency grids. Even when the discontinuities in magnitude are on the order of what could be expected given the experimental uncertainty of these measurements, they lead to sharp features in the reconstructed phase. Given some underlying assumption of smoothness on the true phase response, these features should be considered artifacts of the data collection procedure. Hence, it is desirable to merge the data sets in such a way that these effects are minimized.

Synthesizing a (smooth) data curve from noisy overlapping samples is a topic in its own right. We employed a relatively simple procedure, which is adequate for the current purposes. As a first step, we combined all magnitude measurements—EOS-PD and the three swept-sine calibrations—into a single data set. To do this, we define the "fundamental" frequency grid as the union of all of the experimental frequencies. Next, for each experiment, we interpolated the magnitude data to the fundamental frequencies lying within the frequency interval of that individual experiment. We used piecewise-linear interpolation at this step, and propagated the experimental uncertainty accordingly. Finally, a global data set was formed by computing the average of the magnitude measurements at all frequencies where experiments overlapped. The average was formed by weighting each measurement by the inverse of its associated variance, i.e., the square of its standard uncertainty. In our example, this procedure yields interpolated averaged magnitude data at 800 irregularly spaced frequencies, as shown in Fig. 3.

B. Kramers–Kronig Matrix $\mathbf{K}$

Next we describe our implementation of the Kramers–Kronig operator K and the entries of its matrix representation $\mathbf{K}$. We define the data vector $\mathbf{d}$ and its separation into frequencies and values

$$\begin{aligned}\mathbf{d} &= \{(f_0, y_0), (f_1, y_1), \ldots, (f_N, y_N)\}\\ \mathbf{f} &= \{f_0, f_1, \ldots, f_N\}\\ \mathbf{y} &= \{y_0, y_1, \ldots, y_N\}.\end{aligned}$$

The result of the merging procedure is a piecewise-linear function defined on an arbitrary frequency grid, i.e., it is a C_0-spline interpolating the points $\mathbf{d}$. There are many ways to represent such curves, one being as a linear sum of "hat functions." Given an arbitrary grid of abscissas $\mathbf{f}$, we define the nth hat function $B_n(s;\mathbf{f})$ as the piecewise linear function (see, e.g., [23, Ch. 3])

$$B_n(s;\mathbf{f}) = \begin{cases} \dfrac{s - f_{n-1}}{f_n - f_{n-1}}, & f_{n-1} \le s < f_n \\ \dfrac{f_{n+1} - s}{f_{n+1} - f_n}, & f_n \le s < f_{n+1} \\ 0, & \text{elsewhere.} \end{cases} \tag{31}$$

This definition requires some modifications at the extreme frequencies. We assume that the lowest frequency is dc; $f_0 = 0$. As we are interested in taking the Hilbert transform of $Y(f) = \ln(|h(f)|)$, we know by standard Fourier arguments that this function is even with respect to frequency. Thus, we may augment the data vector to include a reflected frequency and "measurement" about the origin $(f_{-1}, y_{-1}) = (-f_1, y_1)$ and $\mathbf{d} \to (f_{-1}, y_{-1}) \cup \mathbf{d}$. Thereby, $B_0(s;\mathbf{f})$ is defined. Finally, as there are no measurement frequencies beyond f_N, $B_N(s;\mathbf{f})$ is given by the top line of (31) and is zero elsewhere. With these definitions, given tabulated data $\mathbf{d}$, the desired piecewise linear interpolating spline is given by

$$Y(s;\mathbf{d}) = \sum_{n=0}^{N} y_n B_n(s;\mathbf{f}). \tag{32}$$

By construction, $Y(s;\mathbf{d})$ is a simple function defined for all $s > 0$. As such, we may apply the Kramers–Kronig operator (32) analytically. Given a set of target frequencies, we define our discretization of the operator K as the matrix that evaluates the singular integral operator against the interpolant Y formed from the discrete data $\mathbf{d}$ at the desired target frequencies, e.g., $\{f'_m\}$, where the phase has been measured. From (32), we have

$$KY(f'_m) = \sum_{n=0}^{N} y_n K B_n(f'_m). \tag{33}$$

Thus, the m,nth entry of the $\mathbf{K}$ matrix is given by

$$\mathbf{K}_{m,n} = K B_n(f'_m). \tag{34}$$

As $B_n(s;\mathbf{f})$ is continuous for $0 \le n < N$, $KB_n(f')$ will likewise be continuous. The discontinuity in $B_N(t;\mathbf{f})$ at the top frequency $s = f_N$ has the consequence that the image $KB_n(f')$ will have a logarithmic divergence at $f' = f_N$. This divergence is mild and is not observable within our measurement error for $|f'| \le f_{N-1}$. However, it is due to this logarithmic divergence that we enforce the strict inequality $\mathrm{Max}\{f_n\} > \mathrm{Max}\{f'_m\}$ in Section II-B.

It remains to evaluate $KB_n(f')$ in (34). For the sake of clarity, we drop the primes on f in what follows. The operator K applied to a general linear function is fundamental and is given by the identity

$$\begin{aligned}\frac{1}{\pi}\int_{\alpha}^{\beta} \frac{2f}{f^2 - s^2}(ms + b)ds \\ = \frac{m}{\pi} f \ln\left|\frac{\alpha^2 - f^2}{\beta^2 - f^2}\right| - \frac{b}{\pi}\ln\left|\frac{\alpha + f}{\alpha - f}\cdot\frac{\beta - f}{\beta + f}\right|.\end{aligned} \tag{35}$$

For $n < N$, application of K to the hat function B_n is a sum of terms of the form (35) with appropriate definitions of slopes and intercepts m and b. For $0 \le n < N$, substituting (31) into (35) gives

$$\begin{aligned}KB_n(f) = \frac{1}{\pi(f_n - f_{n-1})}\left[\begin{array}{c} f\ln\left|\dfrac{f_{n-1}^2 - f^2}{f_n^2 - f^2}\right| \\ +f_{n-1}\ln\left|\dfrac{f_{n-1}+f}{f_{n-1}-f}\cdot\dfrac{f_n - f}{f_n + f}\right| \end{array}\right] \\ - \frac{1}{\pi(f_{n+1} - f_n)}\left[\begin{array}{c} f\ln\left|\dfrac{f_n^2 - f^2}{f_{n+1}^2 - f^2}\right| \\ +f_{n+1}\ln\left|\dfrac{f_n + f}{f_n - f}\cdot\dfrac{f_{n+1} - f}{f_{n+1} + f}\right| \end{array}\right].\end{aligned} \tag{36}$$

Equation (36) makes sense for $f \notin \{f_{n-1}, f_n, f_{n+1}\}$. At these three points, the logarithmic terms diverge. By construction, however, these divergences cancel and the limit of (35) is finite. For example, the limit as $f \to f_n$ is given by

$$\lim_{f \to f_n} KB_n(f) = \frac{1}{\pi(f_n - f_{n-1})} \left[\begin{array}{c} f_n \ln \left| \dfrac{f_{n-1}^2 - f_n^2}{2f_n} \right| \\ + f_{n-1} \ln \left| \dfrac{f_{n-1} + f_n}{2f_n(f_{n-1} - f_n)} \right| \end{array} \right] - \frac{1}{\pi(f_{n+1} - f_n)} \left[\begin{array}{c} f_n \ln \left| \dfrac{2f_n}{f_{n+1}^2 - f_n^2} \right| \\ + f_{n+1} \ln \left| \dfrac{2f_n(f_{n+1} - f_n)}{f_{n+1} + f_n} \right| \end{array} \right]. \quad (37)$$

We leave the other cases for the readers.

REFERENCES

[1] D. Williams, P. Hale, T. Clement, and C.-M. Wang, "Uncertainty of the NIST electro-optic sampling system," NIST, Boulder, CO, Tech. Note 1535, 2005.

[2] T. S. Clement, D. F. Williams, P. D. Hale, and J. M. Morgan, "Calibrated photoreceiver response to 110 GHz," in *15th Annu. IEEE Lasers Electro-Opt. Soc. Meeting*, Glasgow, U.K., Nov. 10–14, 2002, pp. 877–878.

[3] D. F. Williams, P. D. Hale, T. S. Clement, and J. M. Morgan, "Calibrating electro-optic sampling systems," in *IEEE MTT-S Int. Microw. Symp. Dig.*, May 2001, vol. 1473, pp. 1527–1530.

[4] T. S. Clement, P. D. Hale, D. F. Williams, C. M. Wang, A. Dienstfrey, and D. A. Keenan, "Calibration of sampling oscilloscopes with high-speed photodiodes," *IEEE Trans. Microw. Theory Tech.*, vol. 54, no. 8, pp. 3173–3181, Aug. 2006.

[5] D. C. Degroot, P. D. Hale, M. Vanden Bossche, F. Verbyst, and J. Verspecht, "Analysis of interconnection networks and mismatch in the nose-to-nose calibration," in *ARFTG Conf. Dig.*, Jun. 2000, vol. 55, pp. 116–121.

[6] P. D. Hale, T. S. Clement, K. J. Coakley, C. M. Wang, D. C. DeGroot, and A. P. Verdoni, "Estimating magnitude and phase response of a 50 GHz sampling oscilloscope using the 'nose-to-nose' method," in *55th ARFTG Conf. Dig.*, Jun. 2000, pp. 335–342.

[7] A. Papoulis, *The Fourier Integral and Its Applications*, ser. Electron. Sci.. New York: McGraw-Hill Book, 1962.

[8] F. M. Tesche, "On the use of the Hilbert transform for processing measured CW data," *IEEE Trans. Electromagn. Compat.*, vol. 34, no. 3, pp. 259–266, Aug. 1992.

[9] A. Dienstfrey and L. Greengard, "Analytic continuation, singular-value expansions, and Kramers–Kronig analysis," *Inverse Problems*, vol. 17, pp. 1307–1320, 2001.

[10] J. G. McDaniel and C. L. Clarke, "Interpretation and identification of minimum-phase reflection coefficients," *J. Acoust. Soc. Amer.*, vol. 110, no. 6, pp. 3003–3010, Dec. 2001.

[11] J. Mobley, K. R. Waters, and J. G. Miller, "Finite-bandwidth effects on the causal prediction of ultrasound attenuation of the power law form," *J. Acoust. Soc. Amer.*, vol. 114, no. 5, pp. 2782–2790, Nov. 2003.

[12] H. Dym and H. P. McKean, *Fourier Series and Integrals*. New York: Academic, 1972.

[13] M. Efimchik and B. Levitas, "General properties of the transfer function of stroboscopic converters," *Sov. J. Commun. Technol. Electron.*, vol. 31, no. 4, pp. 110–119, 1986.

[14] R. B. Marks and D. F. Williams, "A general waveguide theory," *J. Res. Nat. Inst. Stand. Technol.*, vol. 97, no. 5, pp. 533–562, 1992.

[15] C. Mittermayer and A. Steininger, "On the determination of dynamic errors for rise time measurement with an oscilloscope," *IEEE Trans. Instrum. Meas.*, vol. 48, no. 6, pp. 1103–1107, Dec. 1999.

[16] I. S. Gradshteyn and I. M. Ryzhik, *Table of Integrals, Series, and Products*, 5th ed. New York: Academic, 1994.

[17] G. B. Arfken and H. J. Weber, *Mathematical Methods for Physicists*, 4th ed. Amsterdam, The Netherlands: Elsevier, 2000.

[18] *"Guide to the Expression of Uncertainty in Measurement,"* BIPM, IEC, IFCC, ISO, IUPAC, IUPAP, and OIML, 1993, pp. 1–101.

[19] R. F. Bauer and P. Penfield, "De-embedding and unterminating," *IEEE Trans. Microw. Theory Tech.*, vol. MTT-22, no. 3, pp. 282–288, Mar. 1974.

[20] D. F. Williams, A. Lewandowski, T. S. Clement, C. M. Wang, P. D. Hale, J. M. Morgan, D. Keenan, and A. Dienstfrey, "Covariance-based uncertainty analysis of the NIST electro-optic sampling system," *IEEE Trans. Microw. Theory Tech.*, vol. 54, no. 1, pp. 481–491, Jan. 2005.

[21] "Agilent Fundamentals of RF and microwave power measurements (part 3)," Hewlett-Packard, Applicat. Note 1449-3, 2003.

[22] J. R. Juroshek, "A direct calibration method for measuring equivalent source mismatch," *Microwave J.*, pp. 106–118, Oct. 1997.

[23] C. de Boor, *A Practical Guide to Splines*, ser. App. Math. Sci.. New York: Springer-Verlag, 1978, vol. 27.

Andrew Dienstfrey received the B.A. degree in mathematics from Harvard University, Cambridge, MA, in 1990, and the Ph.D. degree in mathematics from the Courant Institute of Mathematical Sciences, New York, NY, in 1998.

From 1998 to 2000, he was a Post-Doctoral Scientist with the Courant Institute, where he investigated methods for remote sensing of dielectric properties of superconducting thin films. In 2000, he joined the Mathematical and Computational Sciences Division, National Institute of Standards and Technology (NIST), Boulder, CO. His research interests include theoretical and computational aspects of periodic scattering problems in acoustics and electromagnetics.

Paul D. Hale (M'01–SM'01) received the Ph.D. degree in applied physics from the Colorado School of Mines, Golden, CO, in 1989.

Since 1989, he has been with the Optoelectronics Division, National Institute of Standards and Technology (NIST), Boulder, CO, where has conducted research in birefringent devices, mode-locked fiber lasers, fiber chromatic dispersion, broadband lasers, interferometry, polarization standards, and high-speed opto-electronic measurements. He is currently Leader of the High-Speed Measurements Project in the Sources and Detectors Group. His research interests include high-speed opto-electronic and microwave measurements and their calibration.

Dr. Hale is currently an associate editor for the JOURNAL OF LIGHTWAVE TECHNOLOGY. He was the recipient of the Department of Commerce Bronze, Silver, and Gold Awards, two Automatic RF Techniques Group (ARFTG) Best Paper Awards, and the NIST Electrical Engineering Laboratory's Outstanding Paper Award.

Darryl A. Keenan received the B.S. degree in physics from the University of Colorado at Boulder, in 1996.

In 1989, he joined the National Institute of Standards and Technology (NIST) [then the National Bureau of Standards (NBS)], Boulder, CO, and has since been a member of the Sources and Detectors Group, Optoelectronics Division. He has run optical laser metrology laboratories including low-power continuous wave (CW) from the visible to near infrared, high-power CW at far infrared, Q-switched Nd : YAG at near infrared, and Excimer at ultraviolet to deep ultraviolet. He has worked with colleagues to develop optical fiber connector characterization and to develop a system for measuring detector nonlinearity at 193 nm. His current areas of research include optical laser metrology at 193 and 248 nm and time- and frequency-domain characterization of oscilloscopes using swept sine measurements and calibrated PDs.

Tracy S. Clement (S'89–M'92–SM'05) received the Ph.D. degree in electrical engineering from Rice University, Houston, TX, in 1993. Her Ph.D. research concerned the development and study of novel ultrashort pulse and very short wavelength lasers.

Since 1998, she has been with the Optoelectronics Division, National Institute of Standards and Technology (NIST), Boulder, CO. Her current research interests include the development of measurement systems for high-speed electrooptic components, as well as ultrashort pulse laser measurements. Prior to joining the Optoelectronics Division, she was an Associate Fellow with JILA, in the Quantum Physics Division, NIST, and was an Assistant Professor Adjoint with the Department of Physics, University of Colorado at Boulder. From 1993 to 1995, she was a Director's Post-Doctoral Fellow with the Los Alamos National Laboratory, Los Alamos, NM.

Dr. Clement was the recipient of the Department of Commerce Silver Medal.

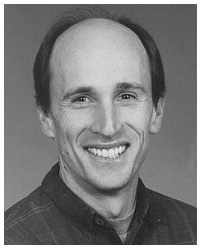

Dylan F. Williams (M'80–SM'90–F'02) received the Ph.D. degree in electrical engineering from the University of California at Berkeley, in 1986.

In 1989, he joined the Electromagnetic Fields Division, National Institute of Standards and Technology (NIST), Boulder, CO, where he develops metrology for the characterization of monolithic microwave integrated circuits and electronic interconnects. He has authored or coauthored over 80 technical papers.

Dr. Williams is currently Editor-in-Chief of the IEEE TRANSACTIONS ON MICROWAVE THEORY AND TECHNIQUES. He was the recipient of the Department of Commerce Bronze and Silver Medals, two Electrical Engineering Laboratory's Outstanding Paper Awards, two Automatic RF Techniques Group (ARFTG) Best Paper Awards, the ARFTG Automated Measurements Technology Award, and the IEEE Morris E. Leeds Award.